Letter

Spatial and magnetic confinement of massless Dirac fermions

Ya-Ning Ren,[1,*] Qiang Cheng,[2,3,*] Si-Yu Li,[1,4] Chao Yan,[1] Yi-Wen Liu,[1] Ke Lv,[1]
Mo-Han Zhang,[1] Qing-Feng Sun,[3,5,6,†] and Lin He[1,‡]

[1]*Center for Advanced Quantum Studies, Department of Physics, Beijing Normal University, Beijing 100875, People's Republic of China*
[2]*School of Science, Qingdao University of Technology, Qingdao, Shandong 266520, China*
[3]*International Center for Quantum Materials, School of Physics, Peking University, Beijing 100871, China*
[4]*College of Materials Science and Engineering, Hunan University, Changsha 410082, People's Republic of China*
[5]*Collaborative Innovation Center of Quantum Matter, Beijing 100871, China*
[6]*Beijing Academy of Quantum Information Sciences, West Bld. #3, No. 10 Xibeiwang East Road, Haidian District, Beijing 100193, China*

(Received 25 March 2021; revised 14 June 2021; accepted 18 October 2021; published 29 October 2021)

The massless Dirac fermions and the ease to introduce spatial and magnetic confinement in graphene provide us unprecedented opportunity to explore confined relativistic matter in this condensed-matter system. Here we report the interplay between the confinement induced by external electric fields and magnetic fields of the massless Dirac fermions in graphene. When the magnetic length l_B is larger than the characteristic length of the confined electric potential l_V, the spatial confinement dominates and a relatively small critical magnetic field splits the spatial-confinement induced atomiclike shell states by switching on a π Berry phase of the quasiparticles. When the l_B becomes smaller than the l_V, the transition from spatial confinement to magnetic confinement occurs and the atomiclike shell states condense into Landau levels (LLs) of the Fock-Darwin states in graphene. Our experiment demonstrates that the spatial confinement dramatically changes the energy spacing between the LLs and generates large electron-hole asymmetry of the energy spacing between the LLs. These results shed light on puzzling observations in previous experiments, which hitherto remained unaddressed.

DOI: 10.1103/PhysRevB.104.L161408

Graphene, with massless Dirac fermions as the low-energy quasiparticles, provides a unique solid-state system to explore many oddball effects of quantum-relativistic matter [1–5]. More importantly, the 1-atom-thick structure of graphene is uniquely amenable to introduce electric and magnetic fields to tune the behaviors of the relativistic fermions. For example, recent experiments demonstrated the confinement of the massless Dirac fermions in graphene into quasibound states via whispering-gallery modes by using circular electronic junctions [6–11], which enable the demonstration of the so-called Klein tunneling [12] at the atomic scale. By further introducing the magnetic fields, it is interesting to find that a small critical magnetic field could lift the angular momentum quantum numbers of the quasibound states by switching on a π Berry phase [13] and a large magnetic field can reshape the electric potentials into wedding-cakelike structures through electron-electron interactions [14]. In the meanwhile, a quite large and unexpected electron-hole asymmetry has been frequently observed in monolayer graphene when both the spatial and magnetic confinements coexist [15–20]. For example, the Fermi velocity for hole could be 30% larger than that for electron. Usually, such a puzzling observation is simply attributed to enhanced next-nearest neighbor hopping in strained structures.

In this Letter, we use scanning tunneling microscopy (STM) to directly probe the interplay between the spatial and magnetic confinements of massless Dirac fermions in graphene. In our experiment, not only the spatial confinement is modified by the magnetic field; our result indicates that the spatial confinement also can strongly affect the effects of the magnetic confinement. When the magnetic length l_B becomes smaller than the characteristic length of the confined electric potential l_V, the transition from spatial confinement to magnetic confinement occurs and the quasibound states gradually condense into Landau levels (LLs) of the Fock-Darwin states in graphene [21]. Our experiments demonstrate that the spatial confinement can change the energy spacing between the LLs and introduce large electron-hole asymmetry between the energy spacing of the LLs.

Our experiments were carried out on electronically decoupled monolayer graphene on a 0.7% Nb-doped $SrTiO_3(001)$ substrate at $T = 4.2$ K (see Supplemental Material for details [22]), as schematically shown in Fig. 1(a). The single-crystal $SrTiO_3$ substrate has been annealed in vacuum to obtain large-area terraces advanced (Fig. S1 [22]). One graphene sheet was first transferred onto the annealed $SrTiO_3$ to further reduce any possible roughness of the substrate and, then, the second graphene sheet was transferred on the first one with a relative twist angle $>10^\circ$. The large twist angle between the two adjacent layers ensures that the topmost graphene sheet is electronically decoupled from the supporting substrate [15–20]. Figure 1(b) shows a representative STM image of the graphene on a $SrTiO_3$ terrace. Our measurement

*These authors contributed equally to this work.
†sunqf@pku.edu.cn
‡helin@bnu.edu.cn

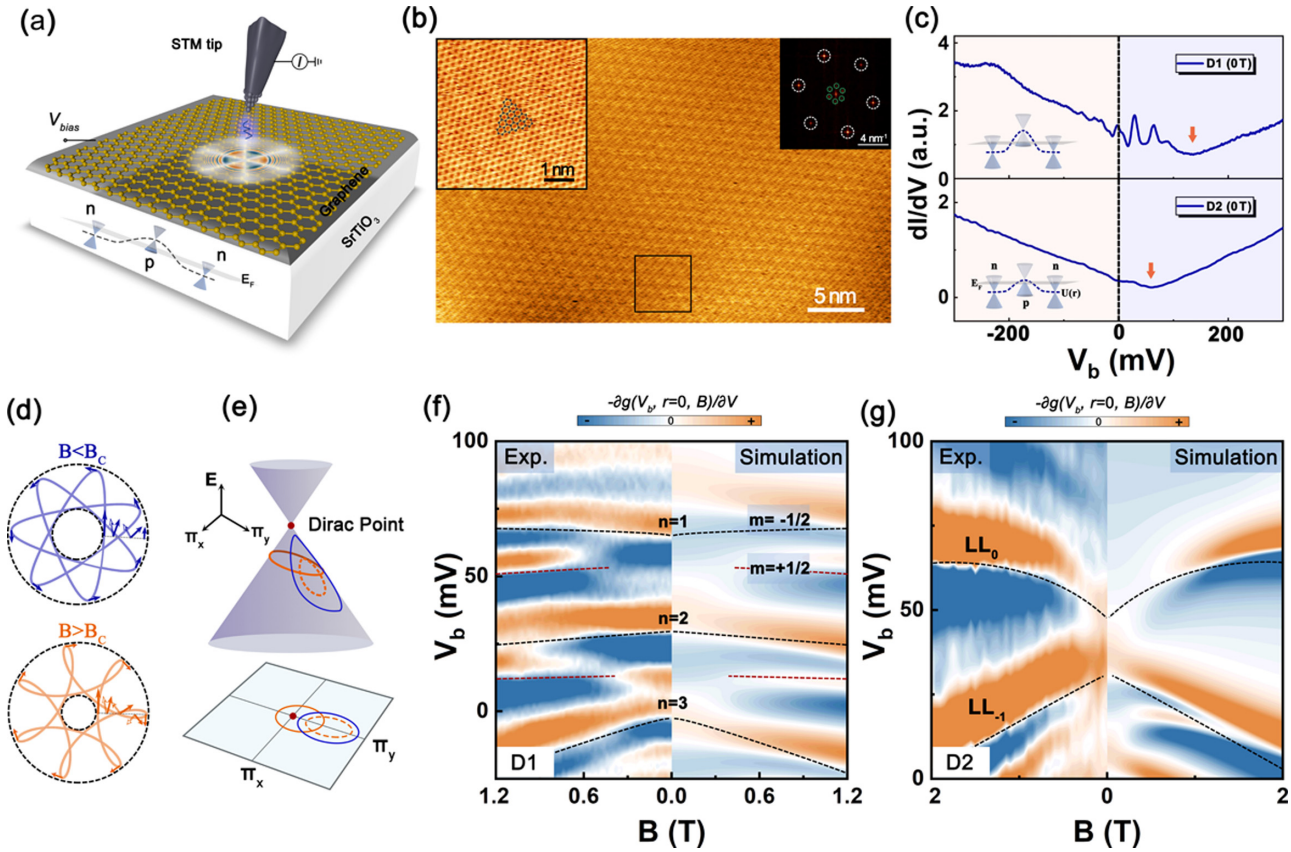

FIG. 1. (a) Sketch of the STM setup. The electric field of the STM tip induces band bending to confine the massless Dirac fermions. (b) A $40 \times 25 - \text{nm}^2$ STM image ($V_{\text{sample}} = 300\,\text{mV}, I = 500\,\text{pA}$) of the D1 region. The topmost graphene sheet decouples from the underlying graphene layer through a large twist angle of about 12°. The left inset shows an atomic-resolved STM image in black rectangle area and the right inset shows the fast Fourier transform (FFT) image. The white circles are reciprocal lattices of graphene and the green circles are reciprocal moiré lattices. (c) STS spectra of monolayer graphene. Dirac points are marked with orange arrows. (d) Schematic diagrams of charge orbits in the circular graphene resonators under different applied magnetic fields. (e) Schematic charge trajectories in momentum space on the Dirac cone for magnetic fields below (blue) and above (orange) the B_C. The orange solid and dashed lines represent $m = +1/2$ and $m = -1/2$ modes, respectively. (f), (g) Differential conductance maps vs magnetic fields B. When magnetic field is larger than the B_C, there is a large and sharp jump in energy of the $m = +1/2$ state in panel (f). No resonances can be observed and the Landau levels are clearly observed in magnetic fields on the order of 0.1 T in the D2 region. The black dotted lines in panels (f) and (g) guide the trend of the experimental energy levels.

demonstrated that both the structure and electronic properties of graphene on a $SrTiO_3$ terrace are quite uniform (Figs. S2 and S3 [22]). However, the Dirac points E_D of graphene on different terraces could be different due to slightly different charge transfer between the substrate and the graphene. Figure 1(c) shows two representative scanning tunneling spectroscopy (STS) spectra recorded in two different regions of the monolayer graphene on different $SrTiO_3$ terraces (labeled as D1 and D2, respectively). The Dirac points E_D in the D1 and D2 regions are at about (147 ± 5) meV and (74 ± 5), meV, respectively. During the STM measurements, the work function difference between the metal STM tip and graphene leads to an electric field acting on graphene and results in the confining potential on the hole, i.e., a circular electronic $p - n$ junction, in graphene below the tip [6,13–16,23–27]. Therefore, clear whispering-gallery resonances, corresponding to tunneling into the circular $p - n$ junction modes at energy $\varepsilon = \mu_0 + eV_b$ (μ_0 is the local Fermi level) [6], are observed in the tunneling spectrum of the D1 region [top panel of Fig. 1(c)]. The energy spacing between the quasibound states is consistent well with that observed previously in the tip-induced graphene resonators [6]. The tip-induced confining potential also depends on the tunneling bias between graphene and the probe tip V_b, as demonstrated explicitly in Ref. [6]. This allows us to tune the spatial confining potential by slightly varying the doping of the graphene monolayer (see Supplemental Material Fig. S4 for details [22]). The dependence of the tip-induced band bending on the V_b makes us almost unable to detect the effect of the confining potential in the zero magnetic-field STS measurements in the D2 region (see Supplemental Material for details [22]) and no resonance can be measured in tunneling spectrum [bottom panel of Fig. 1(c)]. The ability to tune the spatial confining potential allows us to systematically explore the interplay between the spatial and magnetic confinements of the massless Dirac fermions in monolayer graphene, as illustrated below.

A prominent effect of the magnetic fields on the quasibound states is the π shift of the Berry phase [13,28,29]. At zero magnetic field, the quasibound states with opposite angular momenta $\pm m$ are degenerate [Fig. 1(d), top] and their

corresponding momentum-space loops [Fig. 1(e), blue curve] do not enclose the origin. Therefore, the Berry phase of the quasibound states is zero. A small magnetic field breaks the time-reversal symmetry and bends the paths of the $+m$ and $-m$ quasibound states in opposite directions (in our experiment only the angular momenta $\pm 1/2$ states have nonzero wave-function amplitude in the center of the resonators). At a critical magnetic field B_c, the Lorentz force can twist the orbit with angular momentum antiparallel to the magnetic field into a skipping orbit with loops [Fig. 1(d), bottom]. Then, the momentum-space loop encircles the Dirac point [Fig. 1(e), orange curve] and the Berry phase becomes π (the Berry phase of the orbit with angular momentum parallel to the magnetic field is still zero). The π shift of the Berry phase will result in a sudden and large decrease in the energy of the corresponding angular-momentum ($+m$) quasibound states [13,28,29]. Such a feature is clearly observed in our experiment in the D1 region, as shown in Fig. 1(f) [here $g(V_\mathrm{b}, r = 0, B) = dI/dV_\mathrm{b}$ reflects the local density of states (LDOS) in the center of the graphene resonator as a function of V_b and B]. A critical magnetic field lifts the angular momenta $\pm 1/2$ degeneracy of the quasibound states and, then, the spacing between the new states is about one-half the spacing at zero magnetic field [Fig. 1(f), left].

To further understand our experimental result, we theoretically calculated LDOS at $r = 0$. In our calculations, the following Hamiltonian is adopted:

$$H = v_F \boldsymbol{\sigma} \cdot \boldsymbol{\pi} + U(r) + E_D. \tag{1}$$

Here, v_F is the Fermi velocity, E_D is the energy of the Dirac point, $\boldsymbol{\sigma} = (\sigma_x, \sigma_y)$ are pseudospin Pauli matrices, and $\boldsymbol{\pi} = (\pi_x, \pi_y)$ are the kinematic momenta with $\pi_{x,y} = -i\hbar\partial_{x,y} - eA_{x,y}$. The symbol $\hbar$ is Plank's constant divided by 2π. The axial gauges, $A_x = -By/2$ and $A_y = Bx/2$, are used to preserve the rotational symmetry. For simplicity, we consider a fixed circular-shaped p-n junction with a parabolic confining potential $U(r) = -\kappa r^2$. Due to the rotational symmetry, the eigenstates of H can be expressed as $\psi_m(r, \theta) = \frac{e^{im\theta}}{\sqrt{r}}(u_1(r)e^{-i\theta/2}, iu_2(r)e^{i\theta/2})^T$, with the angular momentum quantum number m a half-integer number. The LDOS of the graphene resonator can be expressed as the sum of m-state contributions [6,28]. The π shift of Berry phase and the sudden decrease of energy, as discussed above, can be explained using the Einstein-Brillouin-Keller rule [30–32] starting from the Hamiltonian here (see Supplemental Material for details [22]).

Figure 1(f) shows the simulated LDOS for the D1 region with $v_F = 1.275 \times 10^6\,\mathrm{m/s}$, $\kappa = 32\,\mathrm{eV}/\mu\mathrm{m}^2$ and $E_D = 149\,\mathrm{meV}$. Obviously, the results, including the energy spacing ΔE of the quasibound states at zero magnetic field, the sudden and large reduction in the energy of the angular momentum $+1/2$ states above the B_c, and the value of the $B_C = 2\hbar\mathrm{m}\kappa/[e(E_D - E)] \approx 0.3\,\mathrm{T}$, agree quite well with our experimental results. The good agreement between the experiment and theory indicates that the tip-induced potential is weakly dependent on the tunneling bias in the measured range, $-25\,\mathrm{mV} < V_b < 100\,\mathrm{mV}$. Such a result is reasonable since the variation of the energy induced by the tunneling bias in the measured range, ~125 meV, is much smaller than the work function difference between the metal STM tip and graphene [6,27]. A characteristic length scale for the confining potential $l_V = \hbar v_F/\Delta E$ can be estimated as about 20 nm. Applying a magnetic field B will confine holes in a region of the magnetic length $l_B = [\hbar/(eB)]^{1/2}$. Therefore, for the case that $l_V < l_B$, the spatial confinement dominates and we can observe the quasibound states, as shown in Fig. 1(f). When $l_B < l_V$, a transition from spatial confinement to magnetic confinement occurs and the LLs begin to be observed. In the D1 region, the characteristic Landau quantization of monolayer graphene is observed for $B > 1.4\,\mathrm{T}$, which also agrees well with the estimated l_V above. In the D2 region, the effect of the tip-induced confining potential in the zero-field measurement is almost negligible. Therefore, we observe the characteristic LLs of monolayer graphene for the magnetic field on the order of 0.1 T [Fig. 1(g), left]. Such a feature is also reproduced quite well in our calculation when we consider a very weak confining potential with $\kappa = 9\,\mathrm{eV}/\mu\mathrm{m}^2$ and $E_D = 74$ meV, as well as $v_F = 1.1 \times 10^6\,\mathrm{m/s}$. [Fig. 1(g), right]. In graphene monolayer, the Fermi velocity can be strongly modified, more than 3 times, by varying its charge-carrier concentration and dielectric constant of the supporting substrate [33–35]. The slightly difference of the Fermi velocities in the D1 and D2 regions may be generated by the slight variation of the environment embedding graphene.

To further explore the effect of spatial confinement on the magnetic confinement, the STS spectra in a large range of magnetic fields and sample bias V_b are measured [left panels of Figs. 2(a) and 2(b)]. The theoretical Landau quantization with considering the tip-induced potentials is also calculated for comparison [right panels of Figs. 2(a) and 2(b)]. Our result indicates that the spatial confinement strongly affects the magnetic confinement in several aspects in both the D1 and D2 regions (even though there is no observable tip-induced resonance in the zero-field spectra of the D2 region). The first observable effect generated by the interplay between the spatial and magnetic confinements is that the tip-induced potential $-\kappa r^2$, which is a repulsive potential for the electron, inhibits the formation of quasibound states for the electron in the range $B^2 < \frac{16\kappa}{(v_F e)^2}(eV_b - E_D)$ [see Supplemental Material [22] for details]. Therefore, the LLs can appear at the electron band when $B^2 > \frac{16\kappa}{(v_F e)^2}(eV_b - E_D)$, i.e., the magnetic confinement overcomes the repulsive potential, as shown in Figs. 2(a) and 2(b). The second observable effect of the spatial confinement on the Landau quantization is that the zero LL varies slightly with the magnetic field, as shown in Figs. 2(a) and 2(b). In pristine graphene monolayer, we can observe well-defined Landau quantization, $E_n = \mathrm{sgn}(n)\sqrt{2e\hbar v_F^2|n|B} + E_0$, with the LL number $n = 0, \pm 1, \pm 2, \ldots (n > 0$ corresponds to electrons and $n < 0$ to holes), in the presence of high magnetic field. The energy of the zero LL should be independent of the magnetic fields in the absence of the spatial confinement (see Supplemental Material Fig. S6 for details [22]). The variation of the zero LL in the D1 region is much more pronounced than that in the D2 region due to the much stronger confining potential. Our theoretical results, considering both the spatial confinement and magnetic confinement, reproduce quite well the main features of our experiment. In our experiment, we

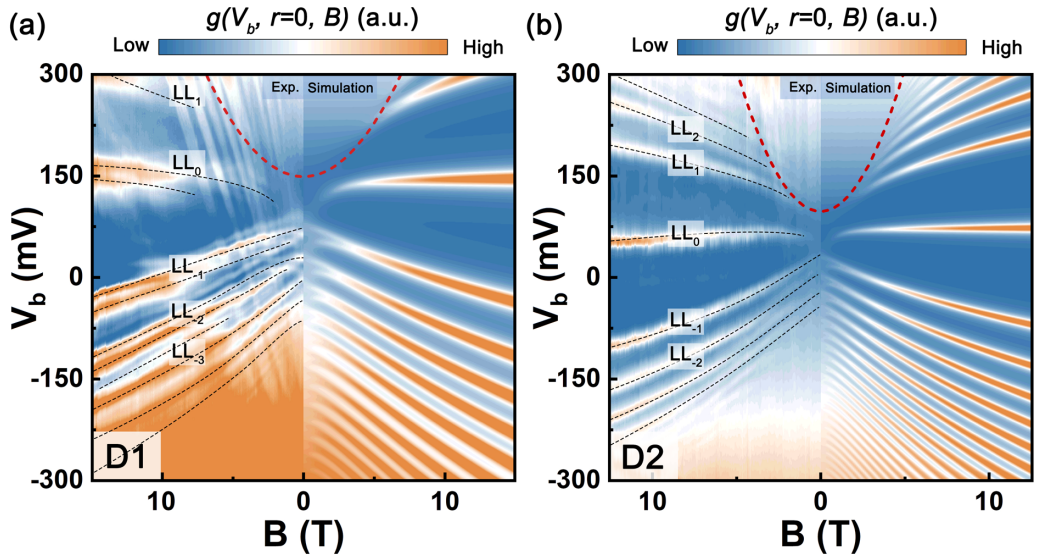

FIG. 2. Panels (a) (left) and (b) (left) correspond to the spectra recorded in the D1 and D2 regions, respectively. Landau levels of massless Dirac fermions are clearly observed in the spectra recorded in high magnetic fields. Panels (a) (right) and (b) (right) show the calculated Landau quantization in the presence of different spatial confinements. The red dotted line is $B^2 = \frac{16\kappa}{(v_F e)^2}(eV_b - E_D)$.

observed slight splitting of the LLs, which may arise from electron-electron interactions that are not taken into account in our theoretical calculations. Besides the LLs, we observe several lines intersecting the LLs at the Fermi level and progressing upward at sharp angles, as shown in Fig. 2. These charging lines arise from Coulomb charging effects, which are generated by shifting quasiparticles in the region beneath the tip into the gaps between the LLs of the adjacent regions [14–16,23,24].

In pristine monolayer graphene, the slope of the data E_n vs $\mathrm{sgn}(n)\sqrt{|n|B}$ directly reflects the Fermi velocity of the massless Dirac fermions and should be a constant.

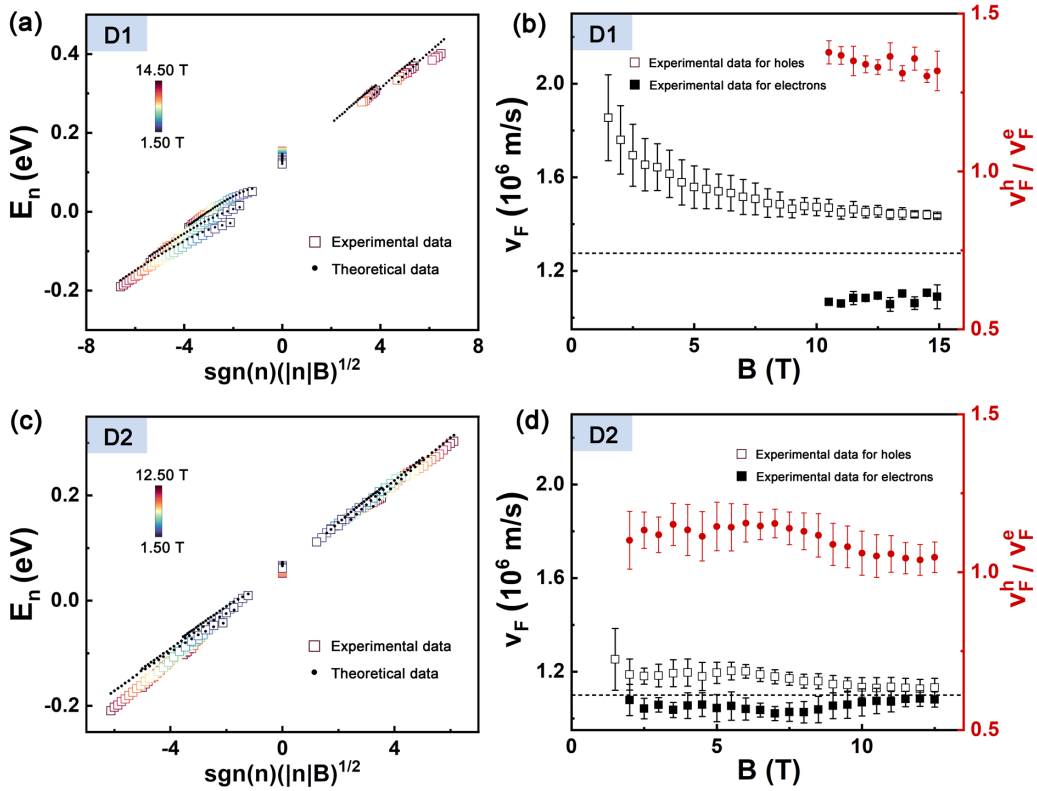

FIG. 3. (a), (c) The Landau level energies against $\mathrm{sgn}(n)(|n|B)^{1/2}$ recorded in the D1 and D2 regions, respectively. The squares represent the experimental data. Black dots correspond to theoretical results extracted from Figs. 2(b) and 2(d) Effective Fermi velocities and v_F^h/v_F^e as a function of magnetic fields. The theoretical result without considering the confining potential is also plotted (dashed lines) for comparison.

However, there are pronounced deviations between the observed Landau quantization in both the D1 and D2 regions and that expected in pristine monolayer graphene, as plotted in Figs. 3(a) and 3(c), because of the existence of the tip-induced spatial potential. To qualitatively show the deviation, the effective Fermi velocity at each magnetic field is extracted according to the energy spacing of the LLs, $v_F = (E_n - E_0)/[\mathrm{sgn}(n)\sqrt{2e\hbar|n|B}]$, and is plotted in Figs. 3(b) and 3(d). The deduced "effective Fermi velocity" for holes is systematically larger than that for electrons, because the tip-induced potential is a confining potential for the hole but it is a repulsive potential for the electron. In the D2 region, the electron-hole asymmetry, as defined by $|v_F^h - v_F^e|/v_F^e$, could be as large as 10%. In the D1 region, the electron-hole asymmetry increases to about 30% due to the relatively stronger tip-induced potential. Generally, the electron-hole asymmetry is much more pronounced in small magnetic fields. Such a result is quite reasonable because the spatial confinement is expected to change the spacing of the LLs, especially for the case that the l_V is comparable to the l_B. In previous STM studies of the Landau quantization in monolayer graphene, similar large electron-hole asymmetry has been frequently observed and is mainly attributed to the enhanced next-nearest neighbor hopping [15–20]. To account for the electron-hole asymmetry observed in the experiment, a large next-nearest neighbor hopping -1 eV is needed to be used as a fitting parameter in the tight-binding model. In our experiment, the strain in graphene is negligible, which removes such a large next-nearest neighbor hopping as the possible origin of the electron-hole asymmetry. By taking into account the effects of the tip-induced potential, our calculation can reproduce quite well the above experimental phenomena (Figs. 2 and 3), indicating that the large electron-hole asymmetry observed in STM studies is mainly arising from the tip-induced potential. The tip-induced potential promotes and resists the formation of the Landau quantization of the hole and electron, respectively, resulting in the giant electron-hole asymmetry.

The Landau quantization of monolayer graphene with different strengths of the confining potential is further calculated (see Supplemental Material [22] and Fig. S7 for details). Figure 4 summarizes the calculated Fermi velocity for electrons and holes as a function of the confining potential. The *n-p-n* and *p-n-p* junctions have opposite confining effects for the electrons and holes, therefore, generating opposite electron-hole asymmetry on the energy spacing, i.e., the effective Fermi velocity, of the LLs. Different charge transfers between the substrate and the graphene can locally generate the *n-p-n* and *p-n-p* junctions in graphene, as reported in previous studies [7,9,36,37]. For example, it has been demonstrated explicitly that a slight structural reconstruction of the Cu surface can lead to a shift of the Dirac point of the graphene about 420 meV [7] and a variation of graphene-Cu separation of about 0.18 nm can generate a shift of the Dirac point of the graphene about 660 meV [9]. This allowed us to test

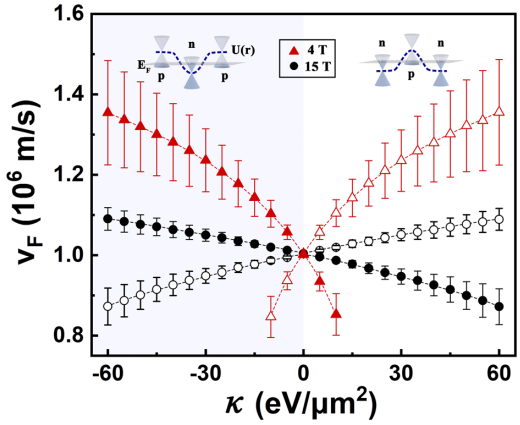

FIG. 4. Theoretical Fermi velocity as a function of the confining potential. The insets schematically show the circular confining potentials. The *n-p-n* and *p-n-p* confining junctions have opposite effects on the Landau quantization for electrons (solid symbols) and holes (open symbols), therefore, generating opposite electron-hole asymmetry.

the above theoretical result in experiment. Our experiment observed opposite electron-hole asymmetry in the *n-p-n* and *p-n-p* junctions of graphene monolayer (see Supplemental Material [22] Figs. S8–S10 for details), as obtained in our theoretical simulation. According to the theoretical result in Fig. 4, the electron-hole asymmetry increases with increasing the strength of the confining potential at a fixed magnetic field, which is consistent with our experimental results obtained in the D1 and D2 regions. For a fixed confining potential, the effect of spatial confinement on the Landau quantization becomes more obvious with decreasing the magnetic fields. Such a result is quite reasonable because the characteristic length of the confining potential l_V is comparable to the magnetic length l_B in small magnetic fields and also agrees well with our experimental results.

In summary, the interplay between the spatial and magnetic confinements of massless Dirac fermions in graphene is systematically explored in this work. Our result demonstrates that a relatively small critical magnetic field lifts the angular momentum degeneracy of the spatial-confined quasibound states by switching on a π Berry phase. In turn, the spatial potential also strongly modifies the magnetic-field induced Landau quantization and generates giant electron-hole asymmetry in the energy spacing between the LLs.

This work was supported by the National Natural Science Foundation of China (Grants No. 11974050, No. 11674029, and No. 11921005) and National Key R and D Program of China (Grant No. 2017YFA0303301). L.H. also acknowledges support from the National Program for Support of Top-notch Young Professionals, support from "the Fundamental Research Funds for the Central Universities," and support from "Chang Jiang Scholars Program."

[1] A. K. Geim and K. S. Novoselov, Nat. Mater. **6**, 183 (2007).

[2] A. H. Castro Neto, F. Guinea, N. M. R. Peres, K. S. Novoselov, and A. K. Geim, Rev. Mod. Phys. **81**, 109 (2009).

[3] M. A. H. Vozmediano, M. I. Katsnelson, and F. Guinea, Phys. Rep. **496**, 109 (2010).

[4] S. Das Sarma, S. Adam, E. H. Hwang, and E. Rossi, Rev. Mod. Phys. **83**, 407 (2011).

[5] M. O. Goerbig, Rev. Mod. Phys. **83**, 1193 (2011).

[6] Y. Zhao, J. Wyrick, F. D. Natterer, J. F. Rodriguez-Nieva, C. Lewandowski, K. Watanabe, T. Taniguchi, L. S. Levitov, N. B. Zhitenev, and J. A. Stroscio, Science **348**, 672 (2015).

[7] C. Gutiérrez, L. Brown, C.-J. Kim, J. Park, and A. N. Pasupathy, Nat. Phys. **12**, 1069 (2016).

[8] J. Lee, D. Wong, J. Velasco Jr, J. F. Rodriguez-Nieva, S. Kahn, H.-Z. Tsai, T. Taniguchi, K. Watanabe, A. Zettl, F. Wang, L. S. Levitov, and M. F. Crommie, Nat. Phys. **12**, 1032 (2016).

[9] K.-K. Bai, J.-J. Zhou, Y.-C. Wei, J.-B. Qiao, Y.-W. Liu, H.-W. Liu, H. Jiang, and L. He, Phys. Rev. B **97**, 045413 (2018).

[10] Z.-Q. Fu, K. K. Bai, Y.-N. Ren, J.-J. Zhou, and L. He, Phys. Rev. B **101**, 235310 (2020).

[11] Z.-Q. Fu, Y.-T. Pan, J.-J. Zhou, K.-K. Bai, D.-L. Ma, Y. Zhang, J.-B. Qiao, H. Jiang, H. Liu, and L. He, Nano Lett. **20**, 6738 (2020).

[12] M. I. Katsnelson, K. S. Novoselov, and A. K. Geim, Nat. Phys. **2**, 620 (2006).

[13] F. Ghahari, D. Walkup, C. Gutiérrez, J. F. Rodriguez-Nieva, Y. Zhao, J. Wyrick, F. D. Natterer, W. G. Cullen, K. Watanabe, T. Taniguchi, L. S. Levitov, N. B. Zhitenev, and J. A. Stroscio, Science **356**, 845 (2017).

[14] C. Gutiérrez, D. Walkup, F. Ghahari, C. Lewandowski, J. F. Rodriguez-Nieva, K. Watanabe, T. Taniguchi, L. S. Levitov, N. B. Zhitenev, and J. A. Stroscio, Science **361**, 789 (2018).

[15] S.-Y. Li, M.-X. Chen, Y.-N. Ren, H. Jiang, Y.-W. Liu, and L. He, 2D Mater. **6**, 031005 (2019).

[16] S.-Y. Li, Y. Su, Y.-N. Ren, and L. He, Phys. Rev. Lett. **124**, 106802 (2020).

[17] A. Luican, G. Li, A. Reina, J. Kong, R. R. Nair, K. S. Novoselov, A. K. Geim, and E. Y. Andrei, Phys. Rev. Lett. **106**, 126802 (2011).

[18] K.-K. Bai, Y.-C. Wei, J. B. Qiao, S.-Y. Li, L.-J. Yin, W. Yan, J.-C. Nie, and L. He, Phys. Rev. B **92**, 121405(R) (2015).

[19] Y. Zhang, S.-Y. Li, H. Huang, W.-T. Li, J.-B. Qiao, W.-X. Wang, L.-J. Yin, K.-K. Bai, W. H. Duan, and L. He, Phys. Rev. Lett. **117**, 166801 (2016).

[20] S.-Y. Li, K.-K. Bai, W. J. Zuo, Y.-W. Liu, Z.-Q. Fu, W.-X. Wang, Y. Zhang, L.-J. Yin, J.-B. Qiao, and L. He, Phys. Rev. Appl. **9**, 054031 (2018).

[21] H.-Y. Chen, V. Apalkov, and T. Chakraborty, Phys. Rev. Lett. **98**, 186803 (2007).

[22] See Supplemental Material at http://link.aps.org/supplemental/10.1103/PhysRevB.104.L161408 for sample preparation, more experimental data, details of calculation, and discussion.

[23] N. M. Freitag, L. A. Chizhova, P. Nemes-Incze, C. R. Woods, R. V. Gorbachev, Y. Cao, A. K. Geim, K. S. Novoselov, J. Burgdörfer, F. Libisch, and M. Morgenstern, Nano Lett. **16**, 5798 (2016).

[24] N. M. Freitag, T. Reisch, L. A. Chizhova, P. Nemes-Incze, C. Holl, C. R. Woods, R. V. Gorbachev, Y. Cao, A. K. Geim, K. S. Novoselov, J. Burgdörfer, F. Libisch, and M. Morgenstern, Nat. Nanotechnol. **13**, 392 (2018).

[25] J. Velasco, Jr., J. Lee, D. Wong, S. Kahn, H.-Z. Tsai, J. Costello, T. Umeda, T. Taniguchi, K. Watanabe, A. Zettl, F. Wang, and M. F. Crommie, Nano Lett. **18**, 5104 (2018).

[26] Y.-W. Liu, Z. Hou, S.-Y. Li, Q.-F. Sun, and L. He, Phys. Rev. Lett. **124**, 166801 (2020).

[27] Y. Jiang, J. Mao, D. Moldovan, M. R. Masir, G. Li, K. Watanabe, T. Taniguchi, F. M. Peeters, and Eva Y. Andrei, Nat. Nanotechnol. **12**, 1045 (2017).

[28] J. F. Rodriguez-Nieva and L. S. Levitov, Phys. Rev. B **94**, 235406 (2016).

[29] Z.-Q. Fu, Y. Zhang, J.-B. Qiao, D.-L. Ma, H.-W. Liu, Z.-H. Guo, Y.-C. Wei, J.-Y. Hu, Q. Xiao, X.-R. Mao, and L. He, Phys. Rev. B **98**, 241401(R) (2018).

[30] Z. Hou, Y.-F. Zhou, X. C. Xie, and Q.-F. Sun, Phys. Rev. B **99**, 125422 (2019).

[31] A. Einstein, Deutshe Phys. Ges. **19**, 82 (1917).

[32] A. D. Stone, Phys. Today **58**(8), 37 (2005).

[33] D. C. Elias, R. V. Gorbachev, A. S. Mayorov, S. V. Morozov, A. A. Zhukov, P. Blake, L. A. Ponomarenko, I. V. Grigorieva, K. S. Novoselov, F. Guinea, and A. K. Geim, Nat. Phys. **7**, 701 (2011).

[34] J. Chae, S. Jung, A. F. Young, C. R. Dean, L. Wang, Y. Gao, K. Watanabe, T. Taniguchi, J. Hone, K. L. Shepard, P. Kim, N. B. Zhitenev, and J. A. Stroscio, Phys. Rev. Lett. **109**, 116802 (2012).

[35] C. Hwang, D. A. Siegel, S.-K. Mo, W. Regan, A. Ismach, Y. Zhang, A. Zettl, and A. Lanzara, Sci. Rep. **2**, 590 (2012).

[36] S.-Y. Li, H.-W. Liu, J.-B. Qiao, H. Jiang, and L. He, Phys. Rev. B **97**, 115442 (2018).

[37] K.-K. Bai, J.-B. Qiao, H. Jiang, H.-W. Liu, and L. He, Phys. Rev. B **95**, 201406(R) (2017).